Low acoustic frequency sensing based on ghost mode of small angle tilted fiber Bragg grating

Jing Tian, Yi-Wu Zuo, Kai-Ming Zhou, Qing Yang, Xiao Hu, and Yang Jiang

***Abstract*—In this paper, we firstly propose a low acoustic frequency sensing system based on small-angle tilted fiber Bragg grating(TFBG) which is used in the sensor head to achieve a high sensitivity. The sensitivity of the proposed diaphragm based acoustic sensing system is theoretically and experimentally proved closely related to the coupling methods and efficiency of ghost mode. In the experiment, the sensing TFBG is tightly bounded on the designed low-frequency polyethylene terephthalate (PET) transducer membrane with a fixed boundary and its ghost mode will have a large wavelength drift and change of amplitude in response to the periodic elastic deformation of the transducer membrane under acoustic pressure. With using the edge filtering demodulation method, the low-frequency acoustic can be effectively and sensitively measured. The theoretical analysis and experimental results indicate that the wavelength and intensity respond linearly to the acoustic pressure. The proposed system can achieve a maximal sensitivity of about 509mV/Pa in the frequency range of 40Hz∼85Hz, a minimum detectable pressure(MDP) of 93μPa/Hz$^{1/2}$@55Hz and signal-to-noise ratio (SNR) of 59 dB. The sensor also demonstrates a flat frequency response within 85Hz∼1500Hz. The sensor operates stably with a peak fluctuation of about ±1mV over 1 h, and about 1.8% for the percentage standard deviation. The proposed acoustic sensor has advantages of high sensitivity at low frequency, high stability and high SNR, simple fabrication, and excellent repeatability.**

***Index Terms*—Optical fiber sensing, tilted fiber bragg grating, acoustic sensing, membrane**

I. Introduction

LOW-FREQUENCY acoustic sensors have been widely used in many fields, such as natural disaster warning[1], medical diagnosis[2] and sonar systems[3]. In recent decades, fiber-optic acoustic sensors (FOAS) have attracted wide attention for obvious advantages of high sensitivity, anti-electromagnetic interference, long-distance detection, low cost and small size in comparison with traditional capacitive and piezoelectric-based electric-type acoustic sensors[4, 5]. Various FOAS techniques are widely investigated including fiber laser[6–9], no-diaphragm interferometer based on Mach Zehnder(MZ)[10], Michelson[11], Sagnac[12]; diaphragm-based fiber acoustic systems such as Fabry Perot (FP) structures[13], fiber coupler[14], tapered fiber[15, 16] and fiber gratings[17–19]. Among these acoustic detection schemes, those based on optical fiber lasers are mainly used for detection of high acoustic frequencies, and they show large noises for low frequencies[6–9], making them ineffective for detection of low acoustic frequencies. Diaphragm-free interferometric acoustic sensors are generally limited in their sensitivities for lacking of a transducer in the design of the sensor head. At present, Fabry Perot (F-P) interferometer (FPI), the typical example of a diaphragm based acoustic sensor, has attracted much attention due to its high sensitivity and compact structure. In this kind of acoustic sensing system, the F-P cavity is formed between the fiber end-face and an elastic diaphragm. With the diaphragm deformed under the action of applied sound pressure, the phase difference between light reflected from the fiber end-face and that from the elastic diaphragm is modulated. The core structure of this kind acoustic sensing system is the F-P cavity and transducer diaphragm. Although the sensitivity of F-P cavity is high, the fabrication process is complex and the measurement range is usually limited, and in order to improve the reflectivity of diaphragms, it is usually necessary to coat the diaphragm with a metal film, which would nevertheless increase the thickness of the diaphragm and introduce a large systematic error.

Other types of FOAS can be based on special optical fiber, including fiber coupler [14], tapered fiber[15], and long-period fiber grating (LPFG)[17–19]. These sensors do not require a reflective transducer diaphragm and are easier to fabricate, only need attachment of the fiber to the transducer diaphragm. Among them, LPFGs have unique advantages over the other special optical fibers based acoustic sensors. They are robust, of small size and light weight and thus of smaller systematic errors. Sensitivity of a LPFG to acoustic waves is attributed to their cladding modes coupling, efficiencies of which can be modulated when the LPFG bends in accordance with the transducer diaphragm under the applied acoustic. However, variation of mode coupling efficiency is still limited and so the ability to further improve the sensitivity for the acoustic is difficult.

It is worth noting that tilted fiber Bragg gratings (TFBGs) couple light from forward core mode to dozens or even hundreds of backward cladding modes, corresponding to resonant dips of narrow linewidth in the transmission spectrum[20–22]. For TFBGs, micro-bending is easy to cause leakage of the cladding modes and changes to their coupling efficiencies. For example taking advantages of their bending sensitivity, scholars realized accelerometers based on TFBGs with excellent performance[23–25]. Even mode coupling method is easy to transfer when receiving an external perturbation, these enable TFBG a high potential in the field of diaphragm based acoustic

This work was supported by the National Natural Science Foundation of China (NSFC) [grant number 61801134, 61835003]; China Scholarship Council[Europe(2022) 1095]. (Corresponding author: Jing Tian)

Jing Tian, Yi-Wu Zuo, Qing Yang, Xiao Hu and Yang Jiang are with the College of Physics, Guizhou University, Huaxi Road, Huaxi District, Guiyang, China (e-mail: jtian1@gzu.edu.cn; 941061337@qq.com; 2631609229@qq.cm; huxiao0410@qq.com; jiangyang415@163.com)

Kai-Ming Zhou is with the Electronic Engineering Department, Aston University, Aston Triangle, Birmingham, B4 7ET , United Kingdom (e-mail: k.zhou@aston.ac.uk)

detection.

In this paper, a low acoustic frequency sensor based on a small angle TFBG is proposed and demonstrated. The small angle TFBG has a strong ghost mode in its transmission spectrum, which is composed of multiple low order cladding modes and sensitive to bending and external perturbation. The proposed sensor consists of a transducer membrane with a fixed boundary and a bounded TFBG. When subject to the acoustic wave, elastic deformation of the membrane is transduced to the TFBG and causes the dramatic wavelength drifts and intensity fluctuations of its ghost mode. Then combined with the edge filtering demodulation method, the sensing system has been proved to be effective for measurement of the low-frequency acoustic. The results show that the theoretical and experimental results are highly consistent, acoustic sensing system proposed in this paper is easy to fabricate, with a good repeatability and stability, high sensitivity.

II. Principles Of Operation

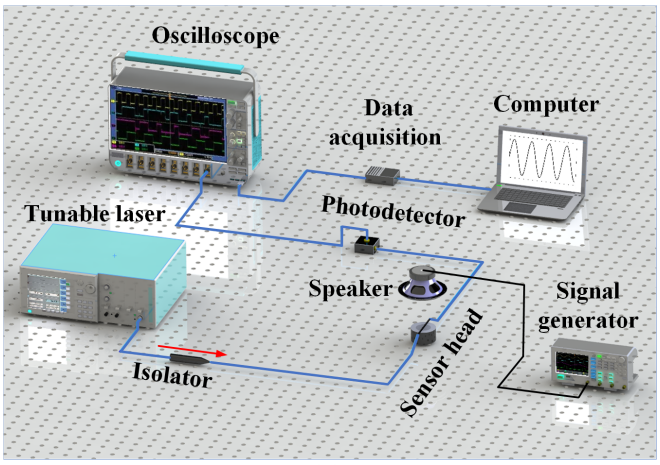

(a)

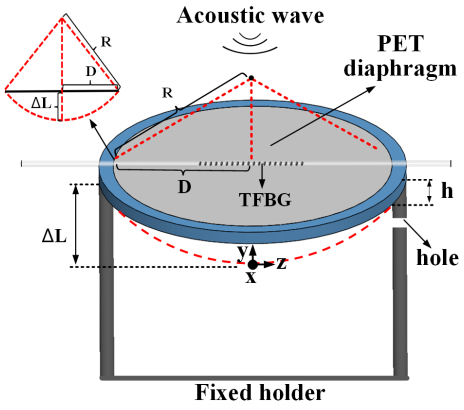

(b)

Fig. 1: Schematic of proposed low acoustic frequency sensing based on small angle tilted fiber Bragg grating (a) The schematic diagram of the proposed acoustic sensing system, (b) sensor head

Fig. 1(a) shows a schematic diagram of the proposed low acoustic frequency sensing system. A narrow line-width output (central wavelength 1552.1nm) from a tunable laser is used to interrogate the sensing TFBG, which is bounded on the transducer membrane shown in Fig. 1(b) During the experiment the central wavelength of the tunable laser is aligned in the linear region of the rising edge of the ghost mode, as shown in Fig. 2. With application of an acoustic signal, the spectrum of TFBG will be dithered, and so be the intensity of the laser passing through the TFBG (central wavelength of ghost mode is 1552nm, tilted angle and length of the TFBG is 5° and 2cm, respectively), which, carrying the acoustic information, is then intercepted by the photodetector (PD) to convert into the electric domain. The signal from the PD is monitored by an oscilloscope and digitalized with the data acquisition (DAQ) card for analysis with a computer. In the experiment, the low-frequency acoustic waves are generated with a speaker driven by a signal generator as shown in Fig. 1 (a). The details of the sensor head is shown in Fig. 1(b), comprising the designed TFBG-PET diaphragm-cylindrical cavity structure.

A. Working principle of the PET

As shown in Fig. 1(b),the designed PET membrane is fixed on the rim of a cylindrical tube, and then TFBG is bounded symmetrically on the central axis of the PET membrane. The first-order natural frequency (f_{00}) of the fixed boundary membrane is given by E.q(1)[26]

$$f_{00} = \frac{10.21h}{2\pi D^2}\sqrt{\frac{E}{12\rho_m(1-\mu^2)}} \tag{1}$$

where D=3cm is the radius of the designed membrane and the thickness h=75μm, Young's modulus of PET is E=2.5GPa, its density $\rho_m = 1.38\times10^3 kg/m^3$ and Poisson's ratio μ=0.39. By taking these parameters into Eq.(1), the natural frequency of the diaphragm is found equal to 57Hz. In addition, the radical (central) deformation of the diaphragm is affected by both the applied acoustic pressure and frequency, and the radial deformation of the diaphragm ΔL is given by [27]

$$\Delta L = \frac{3P(1-\mu^2)D^4}{16Eh^3}\frac{f_{00}^2}{\sqrt{\left(f_{00}^2-f^2\right)^2+4f^2\left(\frac{\xi}{2\rho_m h}\right)^2}} \tag{2}$$

in which f_{00} and ξ are the first natural frequency and damping coefficient of the diaphragm respectively, P and f are the applied acoustic pressure and frequency respectively. It is easy to get from Eq.(2) that, when the applied acoustic frequency approaches the natural frequency, i.e. $f \approx f_{00}$, the diaphragm will have the largest radial deformation due to resonance effect.

B. Working principle of the sensing TFBG

In this acoustic sensing system, the TFBG fixed on transducer membrane is used to demodulate the applied acoustic. As shown in Fig. 1 (b), the effect of the deformation of TFBG can be considered as the combination of the tangential strain along z-axis and radial strain along y-axis. Therefore, when the TFBG senses the tangential strain, its resonant peaks will shift. Supposing the ghost mode consists of n overlapping cladding modes, then its wavelength can be approximated by

the average of the n modes. Then the relationship between the shift of the ghost mode $\Delta\lambda_g$ and tangential strain $\Delta\varepsilon_z$ can be given by

$$\begin{aligned}\Delta\lambda_g &= \sum_{i=0}^{n}\Delta\lambda_{clad,i}/n = \sum_{i=0}^{n}\left(k_{\varepsilon z}^{clad,i}/n\right)\cdot\Delta\varepsilon_z \\ &= k_{gz}\Delta\varepsilon_z\end{aligned} \tag{3}$$

where k_{gz} is the tangential strain coefficient of ghost mode and $\Delta\lambda_{clad,i}$ can be given by

$$\begin{aligned}\Delta\lambda_{clad,i} = &\left(\frac{(n_{clad,i}+n_{core})}{\cos\theta}\frac{d\Lambda}{d\varepsilon}\right. \\ &\left.+\frac{\Lambda}{\cos\theta}\frac{d(n_{clad,i}+n_{core})}{d\varepsilon}\right)\Delta\varepsilon \\ &= k_{\varepsilon}^{clad,i}\Delta\varepsilon_z\end{aligned} \tag{4}$$

In Eq.(4) $n_{clad,i}$ and n_{core} are the effective refractive indices of the i-th cladding mode and the core mode, respectively. Λ is the grating period, θ is tilted angle of the TFBG.

We can see From Eq.(3) that there exists a linear relationship between the wavelength shift of ghost mode $\Delta\lambda_g$ and tangential strain$\Delta\varepsilon_z$. In addition, when the TFBG senses the radial strain, the coupling efficiency will change significantly, this directly leading to variation to the transmission of the ghost mode. According the literature, there exists a linear relationship between the curvature variation and transmission power of the cladding mode in a large range[20, 28, 29]. After a comprehensive analysis, the relationship between the transmission of the ghost mode i_g and curvature variation of the membrane ρ can be given by

$$i_g = i_0 + \sum_{i=0}^{n} k_{\varepsilon\rho}^{clad,i}\rho = i_0 + k_{g\rho}\rho \tag{5}$$

where i_0 is the initial transmission, ρ is curvature of PET membrane, $k_{\varepsilon\rho}^{clad,i}$ is the radial strain coefficient of the ith order cladding mode, $k_{g\rho}$ is the radial strain coefficient of ghost mode.

With the aid of the schematic diagram of acoustic sensor head in Fig.1 (b), we can get the geometric relationship between the curvature ρ, radial deformation of the diaphragm ΔL and the diaphragm radius D, given by $\rho = 1/R = 2\Delta L/\left(D^2+\Delta L^2\right)$. The central radial deformation of the diaphragm ΔL is negligible in comparison with D , i.e. $\Delta L \ll D$, and the geometric expression of ρ can be further reduced as $\rho = 1/R = 2\Delta L/D^2$, Then the intensity changes for ghost mode Δi_g and radial strain $\Delta\varepsilon_\rho$ can be further expressed as

$$\Delta i_g = i_g - i_0 = \sum_{i=0}^{n} k_{\varepsilon\rho}^{clad,i}\frac{2}{D^2}\Delta L = k_{\varepsilon\rho}\Delta L = k_{g\rho}\Delta\varepsilon_\rho \tag{6}$$

Therefore, from Eq.(3) and Eq.(6) we can assert that with the applied acoustic, the wavelength of the ghost mode of TFBG will drift and its intensity fluctuate, all linearly. This provides an effective theoretical basis for the acoustic sensing.

C. Demodulation principle

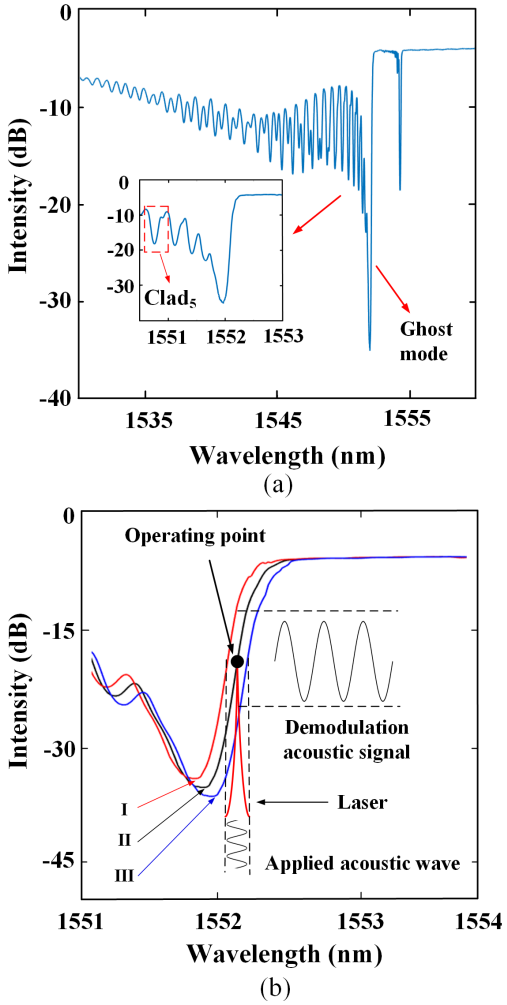

Fig. 2: Transmission spectrum of TFBG: (a)Transmission spectrum of TFBG with small tilt angle, (b)demodulation spectrum.

In this proposed acoustic sensing experimental system, we use a small angle TFBG (with an inclination angle of 5°) as the sensing grating and Fig. 2(a) is its transmission spectrum. With the TFBG having a strong ghost mode, an appropriate point at the rising edge can be used as an operating point. When the sensor is receiving acoustic wave, the ghost mode of the TFBG will have a large wavelength drift and intensity change as well, as shown in Fig. 2 (b) I, II and III. Therefore, by monitoring the intensity of the modulated laser, the acoustic signal can be demodulated.

By combining Eq.(3) , Eq.(6) and the edge filtering demodulation method, the change of the output light intensity ΔI can be given in terms of the tangential strain $\Delta\varepsilon_z$ and radial strain $\Delta\varepsilon_\rho$ by.

$$\Delta I = I_0 k_{gz}\Delta\varepsilon_z + I_0 k_{g\rho}\Delta\varepsilon_\rho \tag{7}$$

Eq.(7) shows that intensity ΔI changes due to wavelength shift of the ghost mode when tensile tangential deformation occurs on the one hand and on the other hand, it changes

due to the variation of the amplitude of the ghost mode when radial deformation occurs. For the device reported in this paper, the acoustic pressure is relevant weak and the tangential deformation $\Delta\varepsilon_z$ is much larger than radial strain$\Delta\varepsilon_\rho$, and thus ΔI changes mainly with the wavelength drift of the ghost mode. Based on analysis from Eq.(2), Eq.(6)and Eq.(7), and definition of $\Delta\varepsilon_z$ and $\Delta\varepsilon_\rho$, ΔI can be linearly related to the applied acoustic pressure P by

$$\Delta I = \mathrm{k}P \tag{8}$$

III. Experimental Results and Discussion

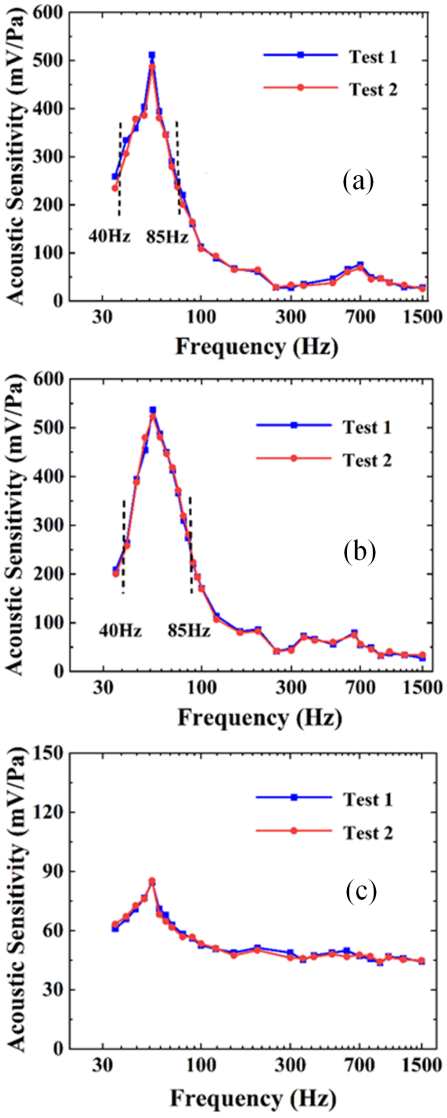

Fig. 3: Frequency response of the proposed acoustic sensing system. (a) frequency response curves under room temperature for the ghost mode. (b) frequency response curves under constant temperature for the ghost mode. (c) frequency response curves under room temperature for a cladding mode.

In the experiment, we tested the response of the proposed sensing system. Firstly, we tested the frequency response and repeatability of the acoustic sensing system. Fig. 3(a) and (b) have shown that the frequency response of the sensor under room temperature (temperature fluctuate ± 0.6°C) and approximate constant temperature (temperature fluctuate ±0.1°C). It can be seen that at room temperature, the experimental results, i.e. the two sweeping curves exhibit only a slight difference, which can arise from variation of the ambient temperature; Fig. 3(b) shows that the two sweep curves almost completely identical for the constant ambient temperature. From Fig. 3(a) and Fig. 3(b) we can see frequency responses is strong and the sensitivity is greater than 245mV/Pa in the frequency range of 40Hz∼85Hz and the maximum sensitivity exceeded 510 mV/Pa. Secondly, we tested the frequency response and repeatability for a cladding mode as shown in Fig. 3(c). Apparently, its frequency responses are weaker and the maximum sensitivity is below 90 mV/Pa. Comparison for the frequency response of the ghost mode and the cladding mode shows that sensitivity of the ghost mode is several times higher than that of the cladding mode. This verifies that ghost mode is composed by multiple cladding modes and this conclusion is also consistent with Eq.(3) and Eq.(6). The two test results with different temperature control shown in Fig.3(a) and (b) indicate that the temperature change has little impact on the sensitivity and frequency response of the sensor, and frequency responses curve shows little change, demonstrating a good repeatability. It can also be seen from Fig.3 that the sensitivity of the sensor to acoustic signals is frequency dependent, with a maximum at 55Hz, approximately equal to the theoretical first-order resonant frequency of 57Hz for this structure. The 2 Hz difference may be attributed by the manufacturing error (including size error for transducer membrane, TFBG pasting introduction error, and ect.). Moreover, the frequency response can be roughly divided into two regions, one with higher sensitivities within 40Hz∼85Hz and with a peak near 55Hz, and another flatter region between 85Hz∼1500Hz.

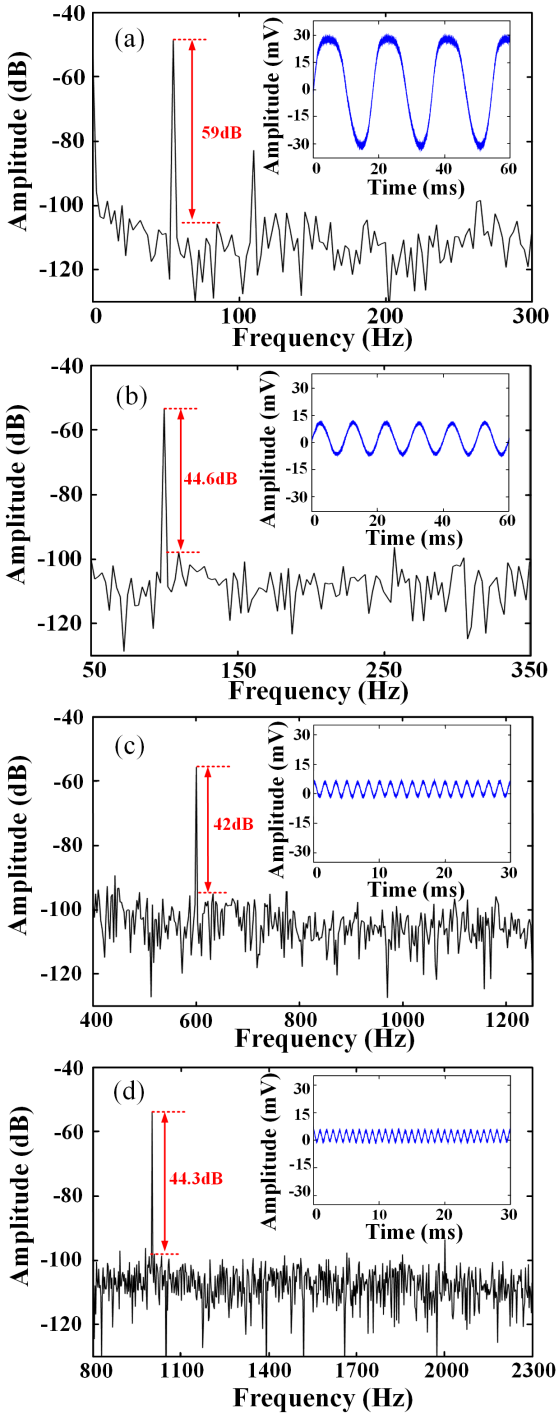

Fig. 4: Time-frequency signal diagram of acoustic signals. (a) at 55Hz, (b) 100Hz, (c)600Hz, (d)1000Hz.

Fig. 4 (a)∼(d) shows the time-frequency signal diagram of acoustic signals detected by the proposed sensor at frequencies of 55Hz, 100Hz, 600Hz and 1000Hz respectively. With an applied acoustic pressure(P) of 76 dB , the corresponding SNR are 59dB, 44.6dB, 42dB and 44.3dB, with the highest SNR near the resonant frequency. The corresponding line-widths(Δf) at 55Hz ,100Hz, 600Hz and 1000Hz are 2.32Hz, 2.02Hz, 2.40Hz, 2.23Hz respectively, giving the minimum detectable acoustic pressures (MDP) of 93μPa/Hz$^{1/2}$@55H, 522μPa/Hz$^{1/2}$@100Hz, 647μPa/Hz$^{1/2}$@600Hz, 516μPa/Hz$^{1/2}$@1000Hz. (The formula for MDP is given by MDP=P/$(10^{SNR/20}\sqrt{\Delta f})$) [30].

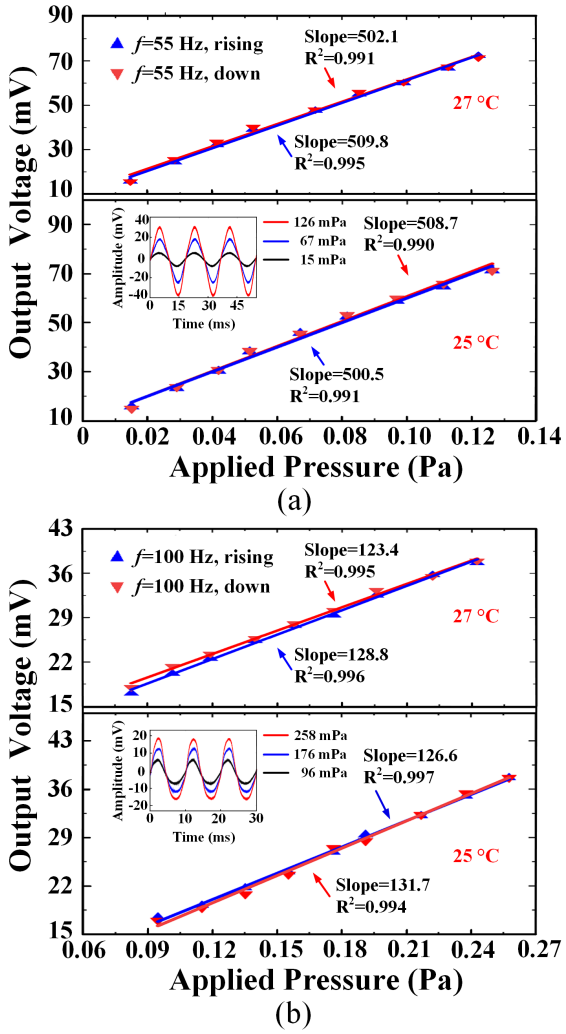

Fig. 5: The sensitivity of the proposed sensor under different applied acoustic pressure and with different temperature. (a)acoustic frequency at 55 Hz, (b) acoustic frequency at 100 Hz

To study the sensitivity of the proposed sensor under different acoustic pressure and different room temperature(25°C and 27°C respectively). We tested 55 Hz acoustic signal of varying intensity and its time domain response is shown in Fig. 5(a). When the applied pressure is increased and decreased, the central part of the (PET) transducer membrane deforms, and thus the output from the PD varies almost linearly, as shown in inset of Fig. 5(a) the sensitivity is 500.5mV/Pa and 508.7mV/Pa respectively for the increased and decreased applied pressure under 25°C. And then the process is repeated with the room temperature set at 27°C. We can see the sensitivity is 509.8mV/Pa and 502.1mV/Pa respectively for the increased and decreased applied pressure. The same experiment process is repeated for acoustic signal of 100 Hz when room temperature is 25°C and 27°C respectively, as

shown in Fig. 5(b), revealing a sensitivity of 126.6mV/Pa and131.7mV/Pa for the rising and down pressures under 25°C. 128.8 mV/Pa and 123.4 mV/pa for the increasing and decreasing pressures respectively under 27°C. From all the experimental results shown in Fig. 5, it can be seen that the response of the proposed sensor has high sensitivity, good linear response and good repeatability, in good agreement with the theoretical results obtained from Eq.(8). And variation of the environmental temperature has a very small impact on the sensitivity.

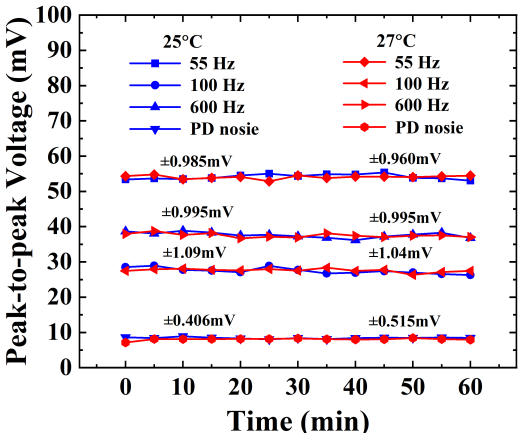

Fig. 6: The stability of the peak voltage time domain signal of the acoustic sensor under different temperatures.

The stability of the acoustic sensor was tested by applying randomly selected acoustic frequencies of 55 Hz,100Hz and 600Hz at room temperature of 25°C and 27°C with a 5min interval for 1 h . Fig. 6 shows that the average fluctuation is about ±1mV over 1 h, with a normalized standard deviation of 1.8% and 1.31% under different temperatures. We reckon that the peak voltage fluctuation is primarily caused by the micro-fluctuation of the room temperature, noises from the light source and the acquisition and demodulation system (such as PD noise, oscilloscope noise and etc). The fluctuation deviation of the peak voltage for PD from Fig. 6 was about ±0.406mV and ±0.515mV over 1 h, and the normalized standard deviation is 0.53% and 0.96% under the temperature of 25°C and 27°C respectively. Variation of the temperature show a slight impact on the noise level of the PD. (in order to reduce the impact caused by the PD noise, we will replace with a balanced photo-detector in future experiments).

To clearly demonstrate the performance of the proposed sensing system, we list results of this paper with those from earlier reports in Table I for comparison. Parameters include acoustic sensitivity and MDP. The comparison shows that the proposed scheme is more sensitive and have smaller MDPs.

IV. Conclusion

In conclusion, we have proposed, comprehensive analyzed, and experimentally demonstrated a low acoustic frequency sensing system which is based on small-angle TFBG. The results demonstrate that the sensitivity of the proposed system is closely related to the coupling methods and efficiency of ghost mode, the theoretical analysis and experimental results indicate that the wavelength and amplitude have a linear response to the acoustic pressure. Experimental results show that the proposed system accurately measures acoustic pressure with excellent repeatability. The sensor has a high sensitive response for frequencies of 40Hz∼85Hz, with a maximal sensitivity of approximately 509mV/Pa, a minimal detectable pressure of 93μPa/Hz$^{1/2}$, and SNR of 59dB. The fluctuation of the PD output is about ±1mV over 1 h. The proposed acoustic sensor has advantages of high sensitivity at low frequency, smaller MDP high stability, simple fabrication, and excellent repeatability.

TABLE I: The comparison with performance of previous FOAS

Sensing structure	Sensitivity	MDP
Fabry–Perot etalon[31]	177.6mV/Pa	530μ Pa/Hz$^{1/2}$
Optomechanical resonator[32]	118.3mV/Pa	232.3μ Pa/Hz$^{1/2}$
Diaphragm-based FP[33]	242.38mV/Pa	17.91μ Pa/Hz$^{1/2}$
Fiber cantilever + FP[34]	88mV/Pa	–
Diaphragm-besed LPFG[19]	–	604.6μ Pa/Hz$^{1/2}$
This work(TFBG)	508.7mV/Pa (at 55Hz) 245∼509mV /Pa (between 40∼85Hz)	93μ Pa/Hz$^{1/2}$

References

[1] S. Shani-Kadmiel, J. D. Assink, P. S. Smets, and L. G. Evers, "Seismoacoustic coupled signals from earthquakes in central italy: Epicentral and secondary sources of infrasound," *Geophysical Research Letters*, vol. 45, no. 1, pp. 427–435, 2018.

[2] T. Ghanayim, L. Lupu, S. Naveh, N. Bachner-Hinenzon, D. Adler, S. Adawi, S. Banai, and A. Shiran, "Artificial intelligence-based stethoscope for the diagnosis of aortic stenosis," *The American Journal of Medicine*, vol. 135, no. 9, pp. 1124–1133, 2022.

[3] J. Liu, M. Liu, C. Sun, Z. Lin, Z. Feng, S. Si, and J. Yang, "Triboelectric hydrophone for underwater detection of low-frequency sounds," *Nano Energy*, vol. 99, p. 107428, 2022.

[4] W. R. Ali and M. Prasad, "Piezoelectric mems based acoustic sensors: A review," *Sensors and Actuators A: Physical*, vol. 301, p. 111756, 2020.

[5] S. A. Zawawi, A. A. Hamzah, B. Y. Majlis, and F. Mohd-Yasin, "A review of mems capacitive microphones," *Micromachines*, vol. 11, no. 5, p. 484, 2020.

[6] Y. Xu, L. Zhang, S. Gao, P. Lu, S. Mihailov, and X. Bao, "Highly sensitive fiber random-grating-based random laser sensor for ultrasound detection," *Optics letters*, vol. 42, no. 7, pp. 1353–1356, 2017.

[7] P. Fan, W. Yan, P. Lu, W. Zhang, W. Zhang, X. Fu, and J. Zhang, "High sensitivity fiber-optic michelson interferometric low-frequency acoustic sensor based on

a gold diaphragm," *Optics Express*, vol. 28, no. 17, pp. 25 238–25 249, 2020.

[8] S. Miao, W. Zhang, Y. Song, and W. Huang, "High-resolution random fiber laser acoustic emission sensor," *Optics Express*, vol. 28, no. 9, pp. 12 699–12 708, 2020.

[9] M. Han, T. Liu, L. Hu, and Q. Zhang, "Intensity-demodulated fiber-ring laser sensor system for acoustic emission detection," *Optics express*, vol. 21, no. 24, pp. 29 269–29 276, 2013.

[10] S. Dass and R. Jha, "Underwater low acoustic frequency detection based on in-line mach–zehnder interferometer," *JOSA B*, vol. 38, no. 2, pp. 570–575, 2021.

[11] J. Jia, Y. Jiang, L. Zhang, H. Gao, and L. Jiang, "Fiber optic dual-ring michelson interferometer-based detection scheme for the measurement of dynamic signals," *Journal of Lightwave Technology*, vol. 37, no. 15, pp. 3750–3755, 2019.

[12] Z. Cheng, J. Zeng, D. Liang, C. Chang, and B. Wang, "Influence of initial phase modulation on the sensitivity of the optical fiber sagnac acoustic emission sensor," *Applied Sciences*, vol. 9, no. 5, p. 1018, 2019.

[13] Z. Qu, P. Lu, Y. Li, X. Fu, W. Zhang, D. Liu, and J. Zhang, "Low-frequency acoustic fabry–pérot fiber sensor based on a micromachined silicon nitride membrane," *Chinese Optics Letters*, vol. 18, no. 10, p. 101201, 2020.

[14] X. Gao, J. Wen, J. Wang, and K. Li, "Broadband acoustic sensing with optical nanofiber couplers working at the dispersion turning point," *Sensors*, vol. 22, no. 13, p. 4940, 2022.

[15] S. Dass and R. Jha, "Tapered fiber attached nitrile diaphragm-based acoustic sensor," *Journal of Lightwave Technology*, vol. 35, no. 24, pp. 5411–5417, 2017.

[16] R. Gao, H. Wang, D. Zhu, G. Fan, H. Yan, P. Wang, Y. Liu, Y. Wang, W. Liu, L. Song, *et al.*, "Acoustic frequency vibration sensor based on tapered sms fiber structure," *Sensors and Actuators A: Physical*, vol. 271, pp. 243–250, 2018.

[17] X. Fu, P. Lu, W. Ni, L. Liu, H. Liao, D. Liu, and J. Zhang, "Intensity demodulation based fiber sensor for dynamic measurement of acoustic wave and lateral pressure simultaneously," *IEEE Photonics Journal*, vol. 8, no. 6, pp. 1–13, 2016.

[18] W. Ni, P. Lu, X. Fu, S. Wang, Y. Sun, D. Liu, and J. Zhang, "Highly sensitive optical fiber curvature and acoustic sensor based on thin core ultralong period fiber grating," *IEEE Photonics Journal*, vol. 9, no. 2, pp. 1–9, 2017.

[19] X. Fu, P. Lu, W. Ni, H. Liao, S. Wang, D. Liu, and J. Zhang, "Spectrum interrogation of fiber acoustic sensor based on self-fitting and differential method," *Optics Express*, vol. 25, no. 4, pp. 4429–4437, 2017.

[20] J. Albert, L.-Y. Shao, and C. Caucheteur, "Tilted fiber bragg grating sensors," *Laser & Photonics Reviews*, vol. 7, no. 1, pp. 83–108, 2013.

[21] Z. Ren, Z. Huang, F. Wang, J. Wu, J. Zhou, Z. Wang, Y. Zhang, Z. Wang, J. Dong, D. Liu, *et al.*, "Tilted fiber bragg grating surface plasmon resonance based optical fiber cadmium ion trace detection," *Sensors and Actuators B: Chemical*, vol. 393, p. 134247, 2023.

[22] C. Shen, D. Liu, X. Lian, T. Lang, C. Zhao, Y. Semenova, and J. Albert, "Microfluidic flow direction and rate vector sensor based on a partially gold-coated tfbg," *Optics Letters*, vol. 45, no. 10, pp. 2776–2779, 2020.

[23] T. Guo, L. Shao, H.-Y. Tam, P. A. Krug, and J. Albert, "Tilted fiber grating accelerometer incorporating an abrupt biconical taper for cladding to core recoupling," *Optics express*, vol. 17, no. 23, pp. 20 651–20 660, 2009.

[24] L. Xie, B. Luo, M. Zhao, O. Deng, E. Liu, P. Liu, Y. Wang, and L. Zhang, "Orientation-dependent optic-fiber accelerometer based on excessively tilted fiber grating," *Optics Letters*, vol. 45, no. 1, pp. 125–128, 2020.

[25] R. Chen, J. He, X. Xu, B. Xu, B. Du, X. Xiao, Y. Wang, C. Liao, X. Weng, L. Liu, *et al.*, "Orientation-dependent accelerometer based on a highly localized fiber bragg grating," *Optics & Laser Technology*, vol. 164, p. 109464, 2023.

[26] Z. Xiang, W. Dai, W. Rao, X. Cai, and H. Fu, "A gold diaphragm-based fabry-perot interferometer with a fiber-optic collimator for acoustic sensing," *IEEE Sensors Journal*, vol. 21, no. 16, pp. 17 882–17 888, 2021.

[27] W. Ni, P. Lu, X. Fu, W. Zhang, P. P. Shum, H. Sun, C. Yang, D. Liu, and J. Zhang, "Ultrathin graphene diaphragm-based extrinsic fabry-perot interferometer for ultra-wideband fiber optic acoustic sensing," *Optics express*, vol. 26, no. 16, pp. 20 758–20 767, 2018.

[28] P. Kisała, D. Harasim, and J. Mroczka, "Temperature-insensitive simultaneous rotation and displacement (bending) sensor based on tilted fiber bragg grating," *Optics express*, vol. 24, no. 26, pp. 29 922–29 929, 2016.

[29] X. Dong, H. Zhang, B. Liu, and Y. Miao, "Tilted fiber bragg gratings: Principle and sensing applications," *Photonic Sensors*, vol. 1, pp. 6–30, 2011.

[30] L. Xin, C. Chen, D. Zhi-Fei, D. Xin, H. Xin-Yu, and Q. Zhi-Mei, "Fiber-optic microphone based on bionic silicon micro-electro-mechanical system diaphragm br," *ACTA PHYSICA SINICA*, vol. 71, no. 9, 2022.

[31] J. Chen, C. Xue, Y. Zheng, L. Wu, C. Chen, and Y. Han, "Micro-fiber-optic acoustic sensor based on high-q resonance effect using fabry-pérot etalon," *Optics Express*, vol. 29, no. 11, pp. 16 447–16 454, 2021.

[32] M. Yao, Y. Zhang, X. Ouyang, A. P. Zhang, H.-Y. Tam, and P. Wai, "Ultracompact optical fiber acoustic sensors based on a fiber-top spirally-suspended optomechanical microresonator," *Optics Letters*, vol. 45, no. 13, pp. 3516–3519, 2020.

[33] S. E. Hayber, T. E. Tabaru, S. Keser, and O. G. Saracoglu, "A simple, high sensitive fiber optic microphone based on cellulose triacetate diaphragm," *Journal of Lightwave Technology*, vol. 36, no. 23, pp. 5650–5655, 2018.

[34] S. Wu, L. Wang, X. Chen, and B. Zhou, "Flexible optical fiber fabry–perot interferometer based acoustic and mechanical vibration sensor," *Journal of Lightwave Technology*, vol. 36, no. 11, pp. 2216–2221, 2018.